Assessment of Hybrid Delta Wing Vortex Flow Investigation -Part I at Subsonic Conditions

Dominik Sedlacek, Christian Breitsamter, Michel Visonneau, Emmanuel Guilmineau, Jeroen Wackers

Assessment of Hybrid Delta Wing Vortex Flow Investigation – Part I at Subsonic Conditions

Dominik Sedlacek * and Christian Breitsamter.†
Technical University of Munich, 85748 Garching, Germany

Michel Visonneau‡ and Emmanuel Guilmineau§ and Jeroen Wackers¶
Ecole Centrale de Nantes - LHEEA-CNRS UMR 6598, 44321 Nantes Cedex 3, France

The dependencies of numerical simulations regarding grid sensitivity and modelling error for vortex dominated flow need particular investigation. In this study, an extensive investigation on the grid sensitivity is conducted and the influence of different turbulence closures is analyzed. For this purpose, a triple- and a double-delta-wing configuration are considered. In a collaboration between the French National Centre for Scientific Research, the Centrale Nantes Engineering School and the Technical University of Munich, simulations were conducted to identify grid and turbulence closure sensitivities. For the grid sensitivity, a comparison of the global force and moment coefficients and of the local flow in the vortex core is shown. From this, it can be concluded that the local flow is more sensitive to grid adaptation than forces and moments. Furthermore, the double-delta-wing configuration seems to be more affected by grid sensitivity. The comparison of k-ω shear stress model, delayed detached eddy simulation and different grids and background closures indicates a lower influence of grid sensitivity to delayed detached eddy simulations than to k-ω shear stress models. A grid convergence represents an important parameter but for vortex dominated flows, it can only be achieved by a local convergence for the vortex core flow is of primary importance as vortex core flow characteristics strongly determines the accuracy of the moment prediction.

I. Introduction

Computational Fluid Dynamics (CFD) are widely spread in aerospace research and design of aircraft. However, for complex flow phenomena occurring in vortex dominated flow fields around highly-agile aircraft, the accuracy and the efficiency of numerical methods are promising but there is still room for further enhancement [1]. Hybrid-delta wings present many assets for the aerodynamic design of high agility aircraft. The flight envelope of such high performance aircraft has to include not only an efficient supersonic performance but also acceptable transonic cruise and high agile maneuverability at subsonic speeds. Therefore, high agility aircraft have to cover a wide range of different and partly contrary flight conditions. Such configurations typically feature moderately to highly swept wings with leading edges varying from small radii to sharp edges. This allows the exploitation of vortex related flow phenomena, such as non-linear lift increase and more resilient vortex systems [2].

Hybrid-delta wing configurations combine the advantages of nonslender and slender wings. These wings are split in sections with different leading-edge sweep. This leads to the development of multiple leading-edges vortices (LEV) which can interact with each other and display superior flight mechanics stability characteristics compared to single vortices [3]. In experimental investigations on similar configurations as the ones investigated here, it is shown that two primary vortices separate at double- and triple-delta-wing configurations [3]. The vortex developing in the front highly swept region is called the inboard vortex (IBV) and the vortex developing at the medium swept leading edge is called midboard vortex (MBV). These vortices interact with each other. With increasing angle of attack (AoA), a rising adverse pressure gradient towards the trailing edge results in a destabilization of the vortex up to vortex breakdown [4]. For vortices developing at slender leading-edge sections, the breakdown can be characterized by an abrupt change in the aerodynamic coefficients as well as reversed core flow and strong velocity fluctuations in the vortex core [5]. Therefore,

*Research Associate, Chair of Aerodynamics and Fluid Mechanics, Boltzmannstrasse 15; dominik.sedlacek@tum.de.
†Professor, Chair of Aerodynamics and Fluid Mechanics, Boltzmannstrasse 15; christian.breitsamter@aer.mw.tum.de. Associate Fellow AIAA.
‡CNRS Research Director, Centrale Nantes LHEEA-UMR6598, Nantes; michel.visonneau@ec-nantes.fr
§CNRS Senior Research Associate, Centrale Nantes LHEEA-UMR6598, Nantes; emmanuel.guilmineau@ec-nantes.fr
¶Centrale Nantes Research Engineer, Centrale Nantes LHEEA-UMR6598, Nantes; jeroen.wackers@ec-nantes.fr

the vortex development, the interaction between multiple vortices as well as the breakdown behavior on hybrid delta wings have a significant influence on flight stability characteristics.
Luckring et al. [1] conducted an extensive synthesis of CFD simulations for the F16-XL configuration, which exhibits similarities with the triple-delta-wing configuration considered in this study. Five different hybrid methods combining Reynolds Averged Navier Stokes (RANS) and Large Eddy Simulations (LES) were used. The superiority of hybrid RANS/LES methods over RANS could be shown due to an improved prediction of vortical characteristics like the primary vortex core flow characteristics, secondary vortex characteristics, vortex interaction details, and vortex breakdown[1] . Further simulations on this configuration were provided by Lofthouse [6]. In this case, the used hybrid RANS/LES method was a delayed detached eddy simulation (DDES) applying the Spalart-Allmaras (SA) model as background closure. The use of a rotation correction introduced by [7] compared to the DDES SA without rotation correction show only a minor effect and the differences between the two models affecting local and global aerodynamic data is more pronounced in RANS simulations. For a further comprehension of vortex dominated flows, computational fluid dynamics is a promising technique. A number of studies focus on CFD for vortex dominated flows and the influences of grid sensitivity and turbulence modeling still need to be investigated.

In this study, numerical investigations on low-aspect-ratio multiple-swept wing fuselage configurations were performed to analyze the influence of the grid sensitivity and the numerical method on the vortex formation as well as on the breakdown behavior. The generic configurations and test cases are embedded in the NATO STO AVT-316 task group on "Vortex Interaction Effects". In this context, the Technical University of Munich (TUM), the French National Centre for Scientific Research (CNRS) and the Centrale Nantes Engineering School (ECN) cooperated to guarantee a versatile analysis of grid and turbulence model influences.

II. Configurations

In this study, two hybrid-delta-wing configurations are investigated. The model is composed of a generic fuselage and a generic flat-plate wing with a sharp leading edge. The first test case, the so-called NA1_W1, is a triple-delta-wing plan form, shown in Figure 1a. This plan form consists of three areas: the Levcon, the first section, with a medium leading-edge sweep of $\varphi_1 = 52.5°$, followed by the strake, a highly swept wing section, $\varphi_2 = 75°$ and the trapezoidal main wing section with a leading-edge sweep of $\varphi_1 = \varphi_3 = 52.5°$. The so-called NA1_W2 configuration consists of a highly swept section $\varphi_2 = 75°$ and a main wing with a leading-edge sweep of $\varphi_3 = 52.5°$. The most important geometrical parameters of the two configurations are summarized in Table 1 [3].

Table 1 Geometrical parameters of the NA1_W1 and NA1_W2 configurations.

		NA1_W1 (TC-01-Inc)	NA1_W2 (TC-04-Inc)
c_r	$[m]$	0.802	0.802
s	$[m]$	0.417	0.367
S_{Ref}	$[m^2]$	0.329	0.266
Λ	–	0.15	0.16
l_μ	$[m]$	0.468	0.426
l_1/c_r	–	0.125	–
l_2/c_r	–	0.350	0.475
l_3/c_r	–	0.475	0.475
φ_1	°	52	–
φ_2	°	75	75
φ_3	°	52	52

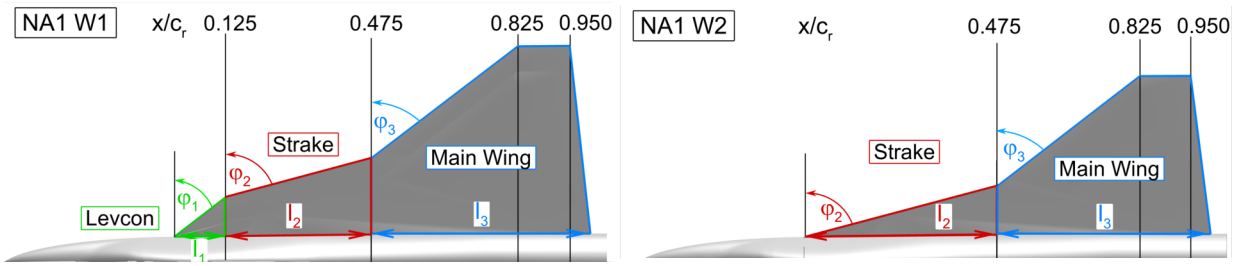

(a) NA1_W1 **(b) NA1_W2**

Fig. 1 Wing planforms

III. Numerical methods

A. TUM

The numerical simulations at TUM are performed with the DLR-TAU-Code, a solver for the Euler or RANS equations on hybrid grids. DDES were also conducted. The idea of the DES, combining RANS and LES, is to model the areas close to the wall and areas with smaller element lengths than the turbulent length scales with a RANS model. The LES model is only used in regions fine enough for LES calculations. This significantly reduces the computing effort and increases the accuracy of the RANS model. The DDES is a modification introduced by Spalart [8, 9]. It maintains the usage of RANS in the boundary layer even if the grid spacing parallel to the wall is smaller than the boundary layer, so the switching to LES is delayed in boundary layers. TAU uses a dual time step method for unsteady simulations. The physical time step is implicitly discretized. The next physical time step is determined iteratively using explicit pseudo time steps. For the RANS part, the turbulence was modelled by the one equation model of Spalart-Allmaras with rotation correction [7, 10, 11]. The unsteady time step for DDES was defined as $\delta_t = 2 \cdot 10^{-5}$ s and the computations converged well within 200 inner iterations per physical time step. As convergence criterion, the Cauchy convergence criterion was used with a control value of $\Delta = 1 \cdot 10^{-6}$ within 10 iterations for lift, drag and pitching moment coefficients as well as maximum eddy viscosity. A second order central scheme as discretization type was employed. The results of the converged DDES solutions are presented in this study. The shown results represent the averaged values of the flow field. The graphs and figures presented in the following study refer to the mean values of the time-accurate CFD computations.

B. ISIS-CFD

The in-house solver ISIS-CFD developed by the CNRS/ECN authors, also available as a part of the FINE™/Marine computing suite distributed worldwide by Cadence Design Systems, is an incompressible multiphase unsteady Navier-Stokes solver mainly devoted to marine hydrodynamics. It is based on a fully-unstructured (face-based) finite volume discretization with specific functionalities needed for multiphase flows and industrial applications (see Queutey & Visonneau [12], Leroyer & Visonneau [13]). The method features several sophisticated turbulence models: apart from the classical two-equation k-ϵ and k-ω models, the anisotropic two-equation Explicit Algebraic Reynolds Stress Model (EARSM), as well as Reynolds Stress Transport Models, are available, see Deng et al. [14], Duvigneau & Visonneau [15] and [16]. All models are available with wall-function or low-Reynolds near wall formulations. Hybrid RANS/LES turbulence models based on Detached Eddy Simulation (DES SST, DDES SST, IDDES) are also implemented and have been thoroughly validated on automotive flows characterized by large separations, see Guilmineau et al. [17] and ships at steady drift [18]. Moreover, the solver accepts sliding and overset grids and features an anisotropic adaptive grid refinement (AGR) functionality ([19], [20]) applied to unstructured hexahedral meshes which will be used extensively here.

In this study, two turbulence models are used: the k-ω SST model [21] and the DDES-SST model [22]. The time step used is $\delta_t = 1.5 \cdot 10^{-4}$ s for the k-ω SST model. The details for DDES-SST will be given further in the section devoted to this computation. The averaging time, tU_∞/c_r varies between 30 and 60 depending on the case. All simulations are performed using the anisotropic automatic grid refinement procedure.

IV. Experimental Methods

Experiments were conducted for the validation of the numerical methods. The wind tunnel A of TUM features an open test section with a cross section of 1.80 $m \times 2.40$ m and a length of 4.80 m. A maximum velocity of $U_{WT} = 65$ m/s can be reached and a turbulence level below 0.4% is provided. For the setting of the angle of attack α, the angle of sideslip β and the roll angle γ, a three component model support is used. The possible range for the angle of attack is $\alpha = 0° - 40°$.

The experimental methods and results of these measurements are also published in [3, 23]. For the measurements, a free stream velocity of $U_\infty = 48$ m/s corresponding to a Reynolds number of $Re = 3.0 \cdot 10^6$ based on the reference length $l_{Re} = 1$ m was used. The following will be a short overview of the most important parameters.

A. Force and moments

The aerodynamic forces and moments were acquired with an internal six-component strain-gauge balance. For axial, lateral, and normal forces, the maximum sustainable loads read 900 N, 450 N, 2500 N, respectively. The maximum sustainable moments are 120 Nm, 160 Nm, 120 Nm for rolling, pitching, and yawing moments, respectively. The measurements were performed with a sampling frequency of $f_m = 800$ Hz for a total acquisition time of $t_m = 10$ s. Ref. [3] presents the accuracy of the aerodynamic coefficients for the applied test setup with respect to repeatability. The force and moment measurements presented in the following refer to the mean values of the acquired series of measurements per angle of attack.

B. Stereo-Particle Image Velocimetry

Stereo-Particle Image Velocimetry (PIV) is used to resolve the flow field above the wing and to obtain all three velocity components. The PIV system consists of two sCMOS cameras with a resolution of 2560×2160 pixels, a double pulsed Nd:Yag laser with a maximum power of 325 mJ per pulse and a wave length of 532 nm and a three axis traversing system next to the wind tunnel test section, see Figure 2. The cameras were placed up- and downstream of the measurement plane with an angle of 60°. The sCMOS sensor planes were tilted by Scheimpflug adapters to meet the Scheimpflug criterion, cf. [24]. The cameras have to be aligned with the laser sheet and were calibrated at an angle of attack of $\alpha = 16°$. For a change in angle of attack, the cameras and laser sheet can be rotated around the Y-axis of the traversing system. Seeding particles with a diameter of ≈ 1 μm were infused into the flow. The shown results are an average of the recorded 400 image pairs per cross section with a sampling frequency of $f_m = 15$ Hz. These were cross-correlated and corrected with the program Davis. The uncertainties of the mean velocity components were quantified as $|u_{err}/U_\infty| < 0.06$ and $|v_{err}/U_\infty| = |w_{err}/U_\infty| < 0.035$ [25].

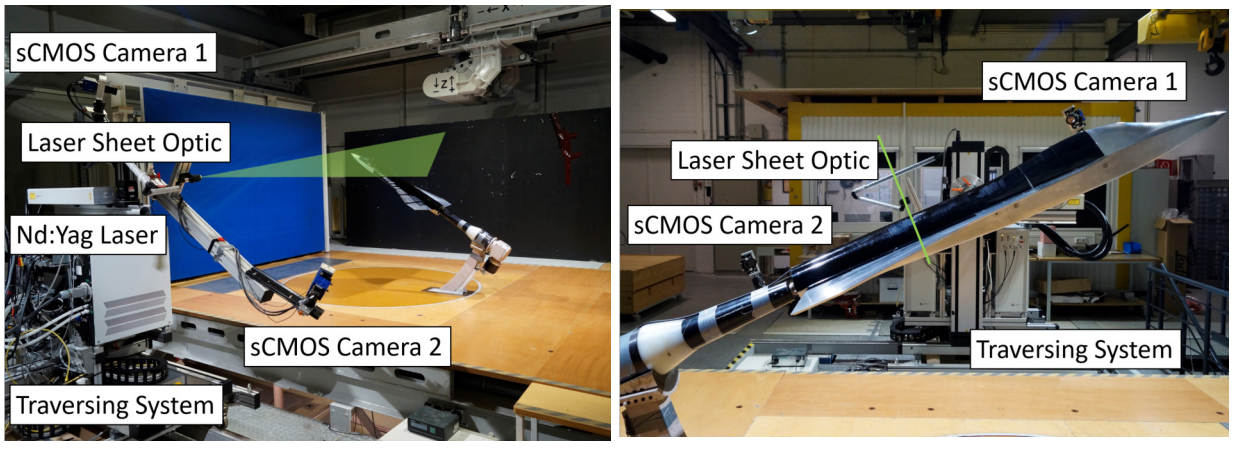

(a) PIV and model setup in test section

(b) Model and indicated laser sheet

Fig. 2 Wind tunnel setup [3]

V. Results

A. Grid sensitivity analysis

1. General context

In order to assess the respective weights of discretization and modelling errors and to evaluate the minimum requirements in terms of local and global grid density needed to maintain the numerical error under control, this study starts with a grid sensitivity analysis performed by CNRS/ECN. The French authors compare a first grid realized by TUM with a series of grids built by them with the help of the anisotropic adaptive grid refinement implemented in their flow solver. Both wing configurations, i.e. NA1_W1 and NA1_W2, are considered at the same angle of attack, $\alpha = 16°$, and the computations are carried out with the k-ω SST turbulence model. To build their series of flow-adapted grids, ECN/CNRS uses the procedure described in [26], which consists in varying systematically the threshold which controls the adaptive grid procedure based on the so-called flux-component Hessian (FCH) criterion computed from Hessians of the pressure and velocity components.

Table 2 provides the values of thresholds, number of cells and faces on the aircraft for both wing configurations for the TUM grid and seven other grids built with the aforementioned grid adaptation. While the global number of cells places the TUM grid between G2 and G1 grids, the local density in the main IBV vortex rather ranks it between G3 and G2. Figs. 3 and 4 illustrate the local crosswise grid densities for all these grids in the section $x/c_r = 0.592$. For both wings, it is obvious that grids G6 to G4 are locally too coarse to describe the main vortices but the last four grids G3 to G0 appear to capture ideally the vortical structures of interest.

Table 2 Number of nodes and cells for the meshes of both configurations.

		NA1_W1			NA1_W2		
		Nb of cells $\times 10^6$	Nb of faces on the aircraft $\times 10^5$	Threshold	Nb of cells $\times 10^6$	Nb of faces on the aircraft $\times 10^5$	Threshold
Hexpress+AGR	G0	87.8	11.9	0.11448	73.4	10.9	0.11448
	G1	76.5	11.0	0.12033	61.4	10.0	0.12033
	G2	32.8	8.2	0.16044	34.0	7.0	0.16044
	G3	19.9	5.6	0.22690	19.6	5.5	0.22690
	G4	18.9	5.4	0.24066	18.9	5.2	0.24066
	G5	16.7	5.0	0.32088	16.1	5.0	0.32088
	G6	14.3	4.6	-	15.3	4.8	-
TUM	TUM	52.0	5.7	-	62.5	7.8	-

2. Forces and moments

Based on the previous grids, Figs. 5a and 5b show the grid convergence of the drag coefficient for both wings. The four last adapted grids (in Figs. from right to left) lie in the asymptotic range, like the TUM grid. Therefore, the difference between the computed drag coefficient and the measurements (in blue) is unequivocally due to a modelling error associated with the linear isotropic $k - \omega$ SST model. The drag and lift are over-estimated for NA1_W1 and under-estimated for NA1_W2, a better agreement being observed for the NA1_W2 wing configuration. It is also reassuring to observe that the results obtained on the non-adapted TUM grid are in perfect agreement with that obtained in case of grid adaptation. Figs. 7 to 10, showing the grid convergence of the individual viscous and pressure components of the drag and lift for both wings, illustrate a well-known result, that the viscous component is significantly less sensitive to the grid discretization than the pressure component.

3. Local Flow

The previous section established that the drag and lift were not significantly affected by the grid density for this specific angle of attack, whatever the considered wing. This finding is confirmed by Figs. 14 and 15 which show

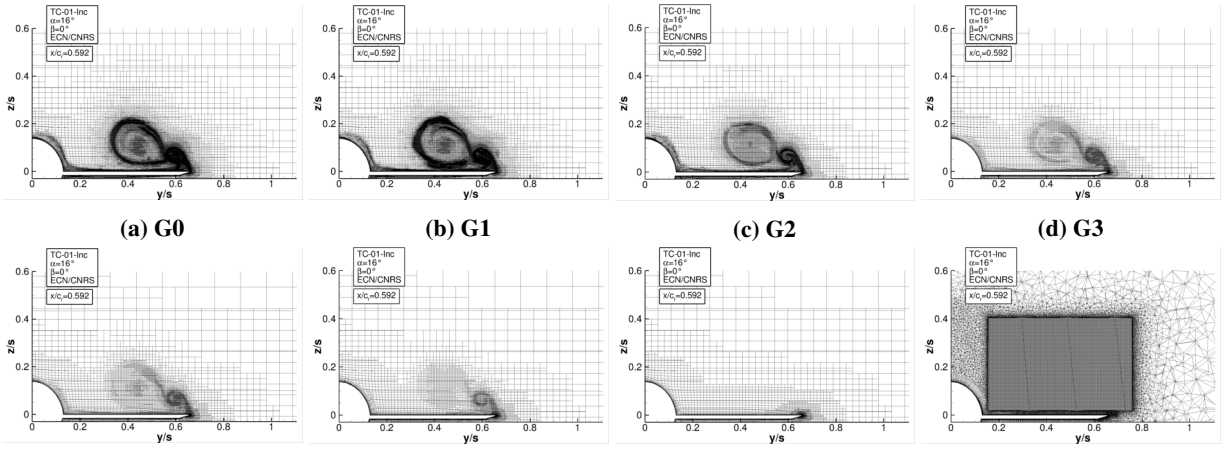

(a) G0 (b) G1 (c) G2 (d) G3

(e) G4 (f) G5 (g) G6 (h) TUM

Fig. 3 Mesh at $x/c_r = 0.592$ vs the size of mesh for the NA1_W1 geometry.

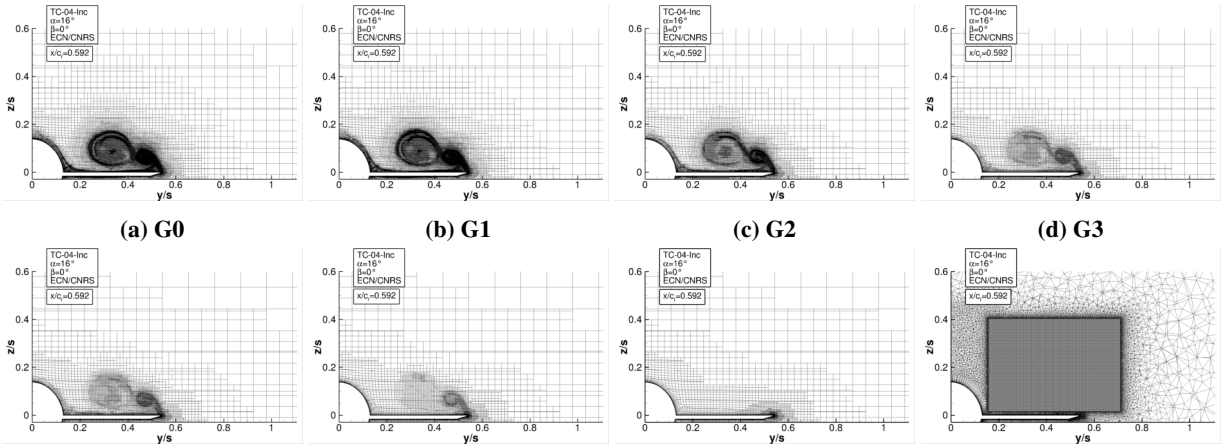

(a) G0 (b) G1 (c) G2 (d) G3

(e) G4 (f) G5 (g) G6 (h) TUM

Fig. 4 Mesh at $x/c_r = 0.592$ vs the size of mesh for the NA1_W2 geometry.

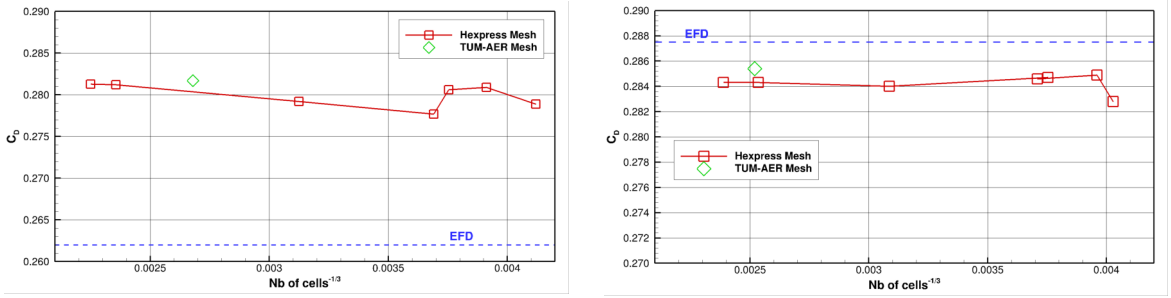

(a) NA1_W1 (b) NA1_W2

Fig. 5 Total drag coefficient vs the size of mesh for $\alpha = 16°$ and $\beta = 0°$; $Re = 3.0 \cdot 10^{-6}$ and $Ma = 0.15$.

for both wings the influence of the grid density on the longitudinal vortical structures represented as iso-surfaces of the dimensionless second invariant $Q^* = Ql_\mu/U_\infty = 50$. The grid influence on the global flow topology and vortex interaction is rather weak. This means that one cannot assess the grid sensitivity on such global flow features. The study on the grid influence should be conducted on more local flow properties. Figs. 16 and 17 show the distributions of

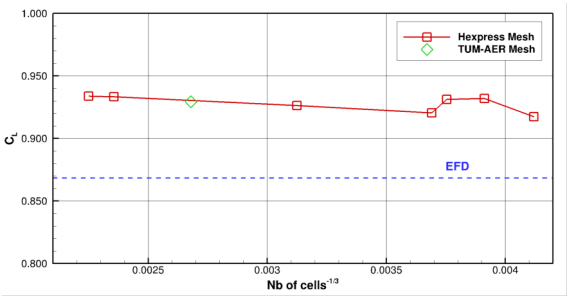

(a) NA1_W1

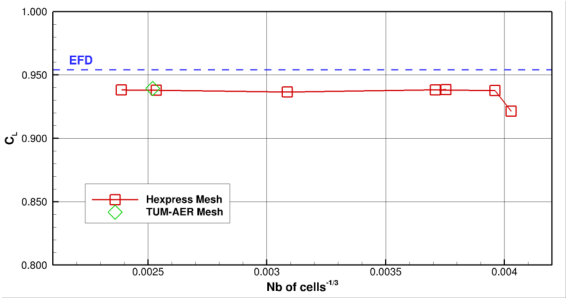

(b) NA1_W2

Fig. 6 Total lift coefficient vs the size of mesh for $\alpha = 16°$ and $\beta = 0°$; $Re = 3.0 \cdot 10^{-6}$ and $Ma = 0.15$.

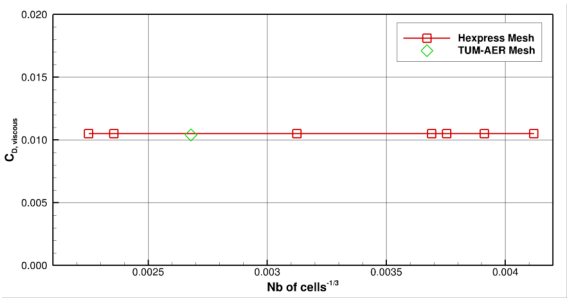

(a) NA1_W1

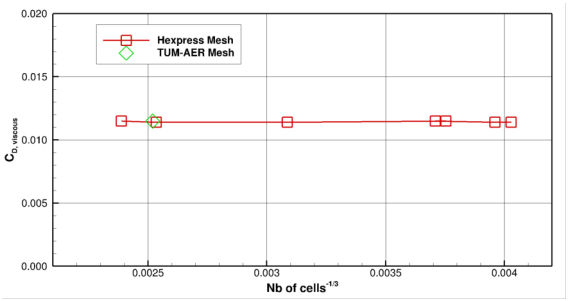

(b) NA1_W2

Fig. 7 Viscous drag coefficient vs the size of mesh for $\alpha = 16°$ and $\beta = 0°$; $Re = 3.0 \cdot 10^{-6}$ and $Ma = 0.15$.

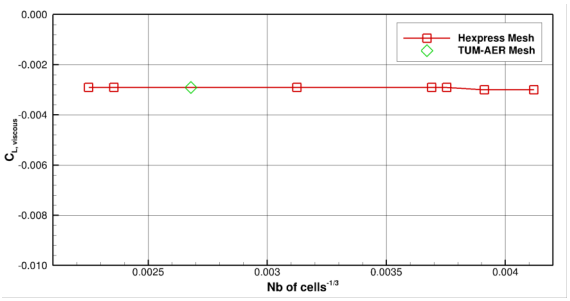

(a) NA1_W1

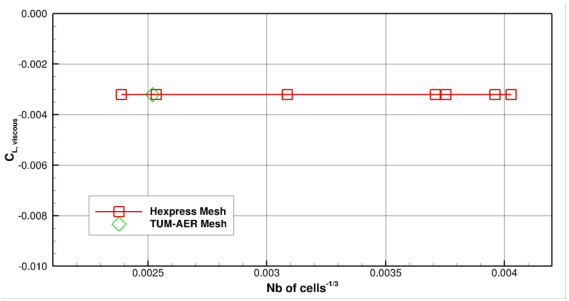

(b) NA1_W2

Fig. 8 Viscous lift coefficient vs the size of mesh for $\alpha = 16°$ and $\beta = 0°$; $Re = 3.0 \cdot 10^{-6}$ and $Ma = 0.15$.

dimensionless axial velocity at section $x/c_r = 0.593$, once again for both wing types. For this angle of attack, a jet-like behavior is observed in the core for both IBV and MBV vortices which is already captured in the coarsest grid G6. The axial velocity is maximum in the core flow of both vortices, with higher values for NA1_W2 than for NA1_W1. The increase of the local grid density leads to higher values of the dimensionless axial velocity in the core of the primary IBV vortex and a better capturing of the secondary MBV vortex. The results obtained on the TUM grid look similar to those obtained on the G4 or G3 grids. They are clearly not grid converged in the core of the vortex at this specific section. This clearly proves that, contrary to the conclusion one might draw from the previous figures, the local core flow computed on grid G3, for instance, is not yet grid-independent, despite the high local density resulting from the use of an efficient local grid adaptation.

Thus, it is important to assess the grid sensitivity on these local flow properties since we have observed that the behavior of the flow in the core of the vortex, notably its longitudinal fluid dynamics stability, will strongly determine the accuracy of the aerodynamic moment prediction. Moreover, to evaluate the ability of turbulence models to capture some of the vortex core flow physics, it is crucial to determine the minimal local grid density and number of points

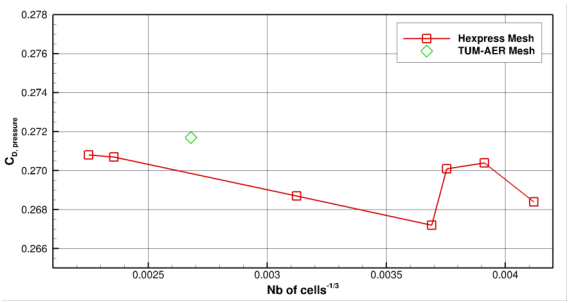

(a) NA1_W1

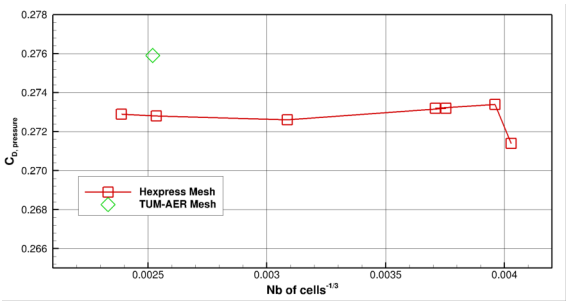

(b) NA1_W2

Fig. 9 Pressure drag coefficient vs the size of mesh for $\alpha = 16°$ and $\beta = 0°$; $Re = 3.0 \cdot 10^{-6}$ and $Ma = 0.15$.

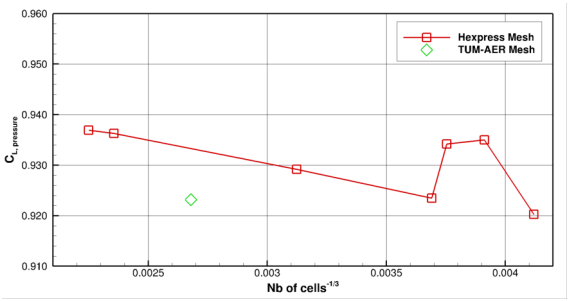

(a) NA1_W1

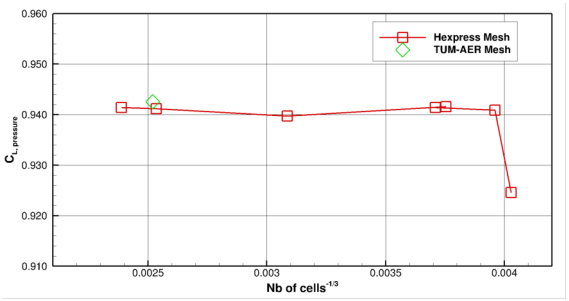

(b) NA1_W2

Fig. 10 Pressure lift coefficient vs the size of mesh for $\alpha = 16°$ and $\beta = 0°$; $Re = 3.0 \cdot 10^{-6}$ and $Ma = 0.15$.

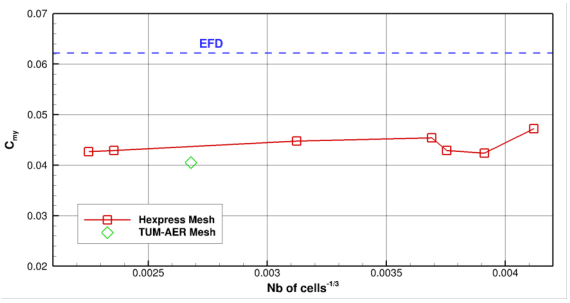

(a) NA1_W1

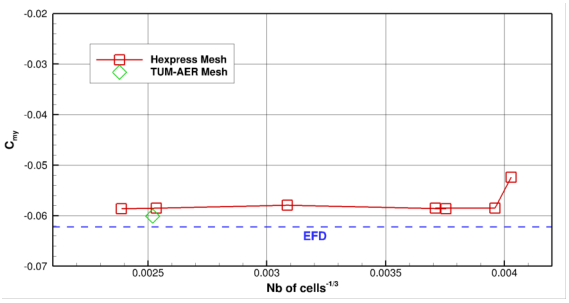

(b) NA1_W2

Fig. 11 Total pitching moment coefficient vs the size of mesh for $\alpha = 16°$ and $\beta = 0°$; $Re = 3.0 \cdot 10^{-6}$ and $Ma = 0.15$.

needed in the core of a vortex for which one can consider that the assessment of turbulence models is no more affected by the discretization error. This is the reason why we conclude this grid sensitivity study by a vortex core analysis (VCA). First of all, in order to comply with the method used in the experiments, the core of the vortex is identified as the maximum of the longitudinal vorticity. Since the vorticity and second invariant depend on the local flow gradient, these indicators might be very sensitive to the local grid density. When the vortex is intense and stable, both approaches provide a core location which is in good agreement. However, when the vortex gets more diffused and less stable, the two detection methods might provide a different core location, which is moreover quite different from the experimental core determined on an experimental grid which is, most of the time, significantly coarser. This vortex core analysis should therefore be conducted with caution. Then, the dimensionless axial velocity component is extracted at the core of each IBV and MBV vortices and compared with the available experimental data.

The Vortex Core Analysis is shown for both wing types in Figs.18 and 19 which display the lateral Y (resp. vertical Z) position of the core of the IBV vortex, the longitudinal velocity component U, the longitudinal vorticity ω_x and the

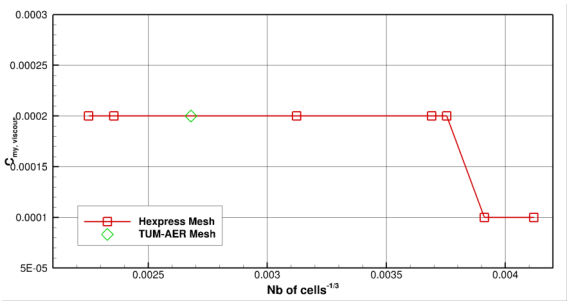

(a) NA1_W1

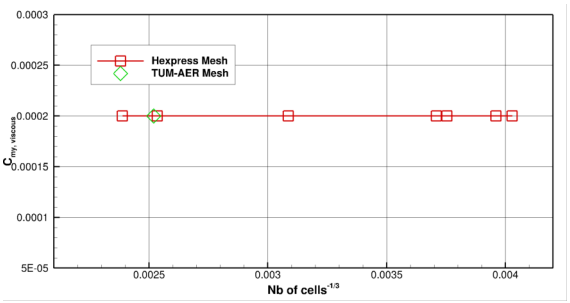

(b) NA1_W2

Fig. 12 Viscous pitching moment coefficient vs the size of mesh for $\alpha = 16°$ and $\beta = 0°$; $Re = 3.0 \cdot 10^{-6}$ and $Ma = 0.15$.

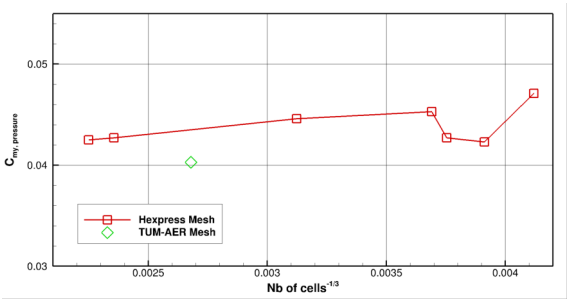

(a) NA1_W1

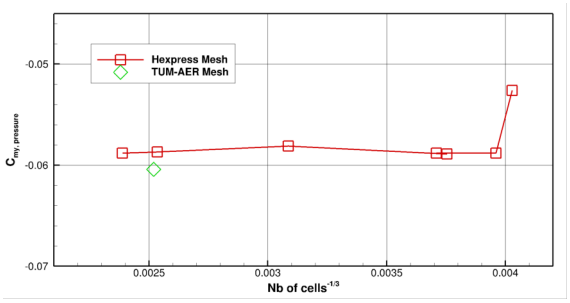

(b) NA1_W2

Fig. 13 Pressure pitching moment coefficient vs the size of mesh for $\alpha = 16°$ and $\beta = 0°$; $Re = 3.0 \cdot 10^{-6}$ and $Ma = 0.15$.

turbulence kinetic energy (TKE) extracted at the core of the IBV vortex. For both wing types, the lateral and vertical positions of the IBV vortex (Figs. 19a and 19b) are not sensitive to the local grid density, except very close to the trailing edge, where the vortex starts to destabilize. For NA1_W1, the axial velocity component is very much dependent on the local grid density during the initial progression of the IBV vortex up to $x/c_r = 0.5$ where a larger spreading can be observed and results from the TUM grid depart from the others. The longitudinal vorticity appears to be very well converged all along the vortex trajectory for all the grids generated by automatic adaptation. Once again, the TUM grid appears to be too coarse to capture the strong velocity gradients present in the core of the IBV vortex, particularly in the initial zone of progression. Finally, the turbulence kinetic energy appears reasonably well converged on the series of adapted grids, which is not true for the TUM grid with a factor two between the two evaluations of the turbulence kinetic energy. However, the global shape of evolution of the turbulence kinetic energy — an initial decay up to $x/c_r = 0.5$ and then an increase up to $x/c_r = 0.85$ — is very similar for the two classes of grids.

For NA1_W2, the longitudinal velocity component U (Fig. 19c) is much more affected by the grid sensitivity, especially close to the onset of the vortex. The maximum value is increased by 16% and converges only for the finest grids G1 and G0. Particularly, the solution computed on the TUM grid is far from being grid-converged before $x/c_r = 0.5$. The same behavior is observed on the longitudinal vorticity (Fig. 19d) which is even more affected by the local grid density, as expected. Finally, one can also observe a less pronounced grid sensitivity for TKE (19e), although the solution on the TUM grid appears outside of the range of the solution obtained on the grids generated by local adaptation from the onset to $x/c_r = 0.5$. The behavior of U, ω_x and TKE reveals that the TUM grid is not well adapted to the onset of the IBV vortex and is probably not sufficiently refined in the region close to the leading edge.

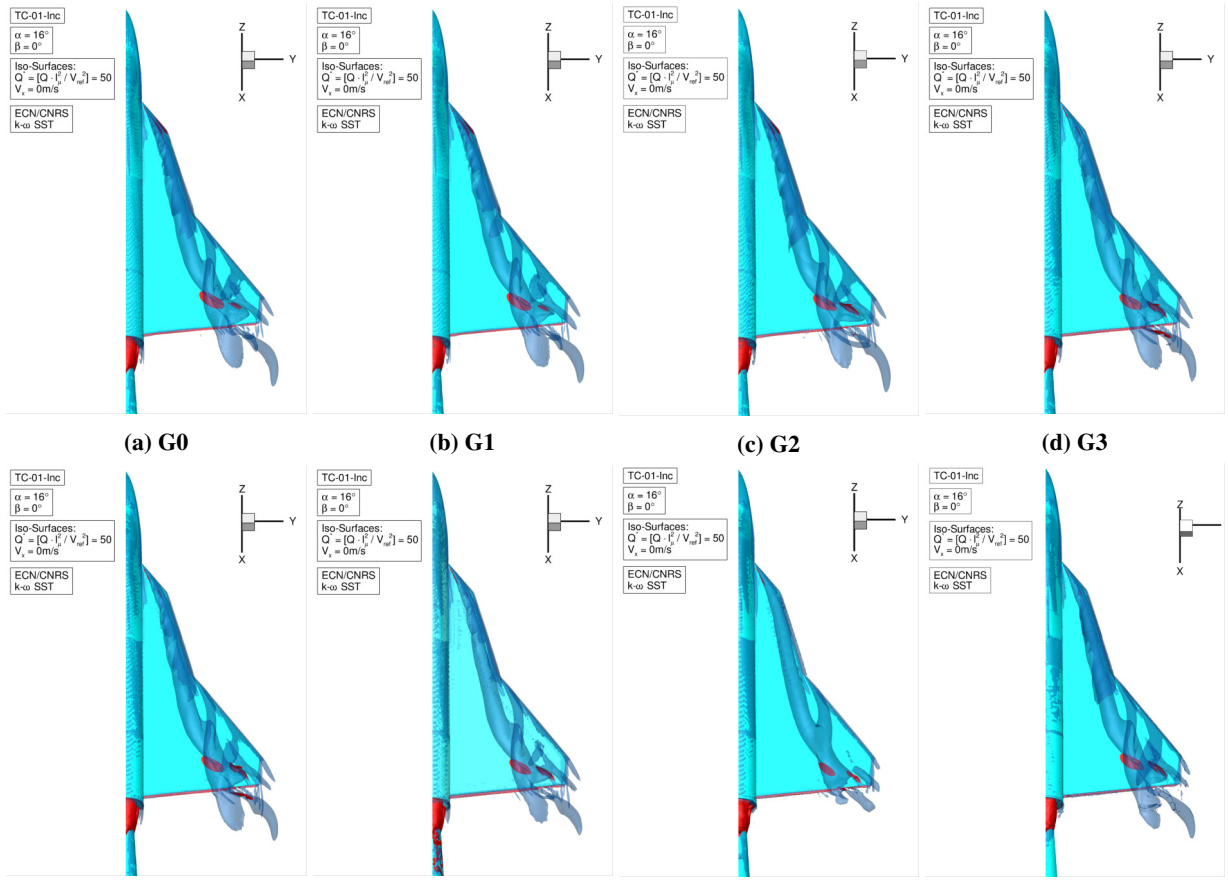

(a) G0 **(b) G1** **(c) G2** **(d) G3**

(e) G4 **(f) G5** **(g) G6** **(h) TUM-mesh**

Fig. 14 3D longitudinal vortices represented by dimensionless Q*=50 surfaces vs the size of mesh for the NA1_W1 geometry for $\alpha = 16°$ and $\beta = 0°$; $Re = 3.0 \cdot 10^{-6}$ and $Ma = 0.15$.

B. Simulation Sensitivity to Solver, Grid and Turbulence Model

1. Description of the hybrid RANS/LES models and computational setup

In the following, the simulation results for both considered configurations at $\beta = 5°$ and $\alpha = 24°$ are compared. The French authors carried out simulations with the k-ω SST and DDES-SST turbulence closures on the grid provided by TUM, named here "TUM" and the grid resulting from the automatic flow adaptation, named here "Hexpress+AGR". The time step used is $\delta_t = 5 \cdot 10^{-5}$ s for the DDES model. The averaging time, tU_∞/c_r varies between 30 and 60 depending on the case, except for the case $\alpha = 24°$ and $\beta = 5°$ for the NA1_W2 geometry where the averaging time is 6.5. All simulations are performed using the automatic grid refinement procedure. The German authors provided in this part their hybrid RANS/LES simulations computed on their "TUM" grid. The considered hybrid RANS/LES model used the SA with rotation correction as background closure (DDES SA). For unsteady dual time stepping, a time step of $\delta_t = 2 \cdot 10^{-5}$ s is used and the results are averaged within $tU_\infty/c_r = 15$ for both configurations. The different setups are compared by means of forces and moments, surface pressure distribution, velocity crossflow sections and vortex core characteristics.

2. Analysis of the computations

Forces and moments. Table 3 shows the data of the force and moment predictions obtained on these different grids for the NA1_W1 configuration. The first two lines of this table illustrate the moderate but non-negligible influence of the local grid density on the forces and moments. The results obtained with the k-ω SST closure on the flow-adapted grid being closer to the measurements, particularly, for the longitudinal characteristics C_D, C_L and C_{my}. In the lateral

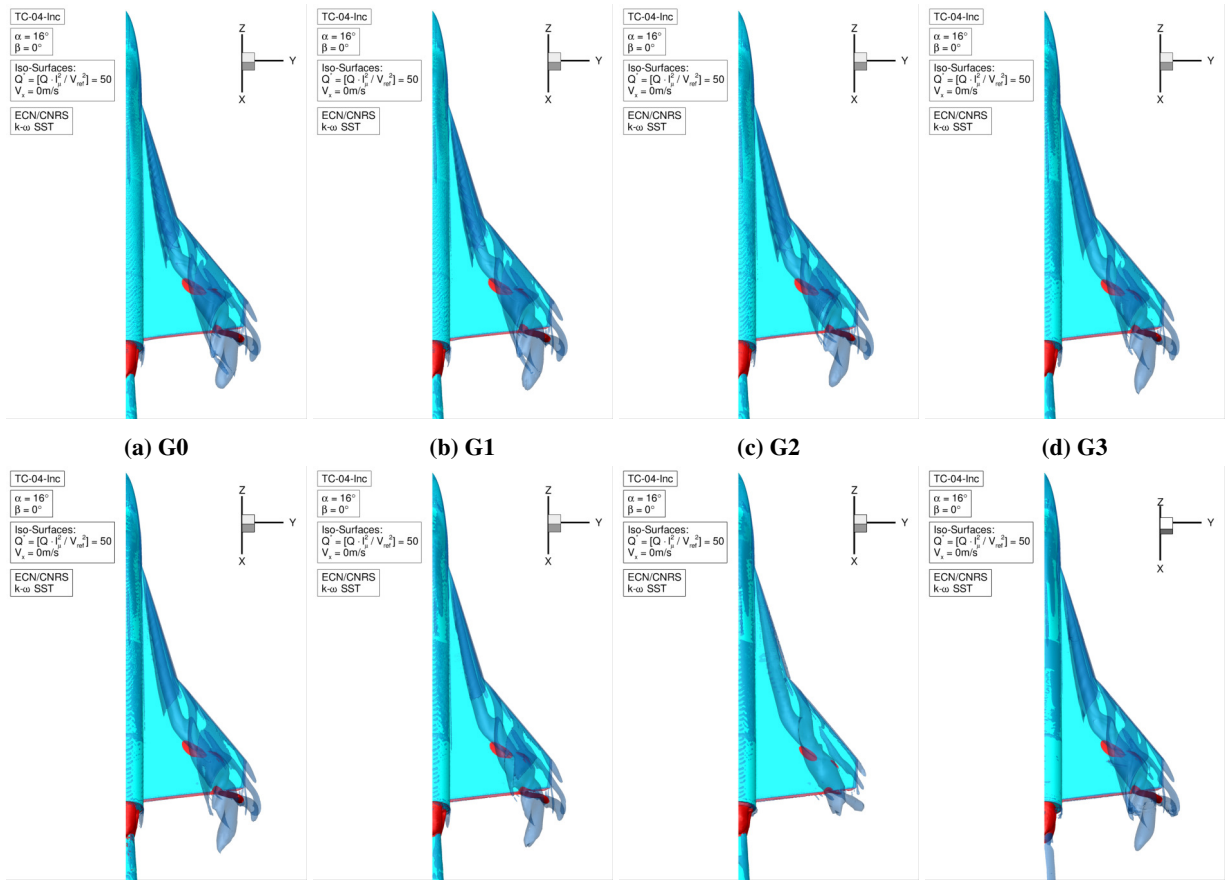

(a) G0 (b) G1 (c) G2 (d) G3

(e) G4 (f) G5 (g) G6 (h) TUM-mesh

Fig. 15 3D longitudinal vortices represented by dimensionless Q*=50 surfaces vs the size of mesh for the NA1_W2 geometry for $\alpha = 16°$ and $\beta = 0°$; $Re = 3.0 \cdot 10^{-6}$ and $Ma = 0.15$.

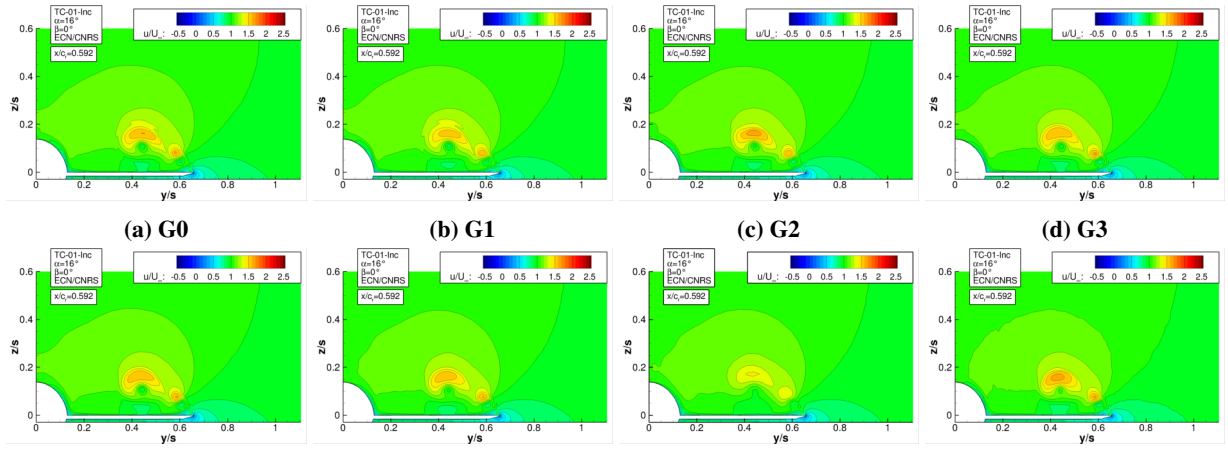

(a) G0 (b) G1 (c) G2 (d) G3

(e) G4 (f) G5 (g) G6 (h) TUM-mesh

Fig. 16 Dimensionless axial velocity at $x/c_r = 0.592$ vs the size of mesh for the NA1_W1 geometry for $\alpha = 16°$ and $\beta = 0°$; $Re = 3.0 \cdot 10^{-6}$ and $Ma = 0.15$.

characteristics, the disappointing behavior of the k-ω SST simulations for the Hexpress+AGR is similar to the TUM grid. No setup predicts a rolling moment coefficient C_{mx} similar to the experiment. Therefore, this discrepancy in the

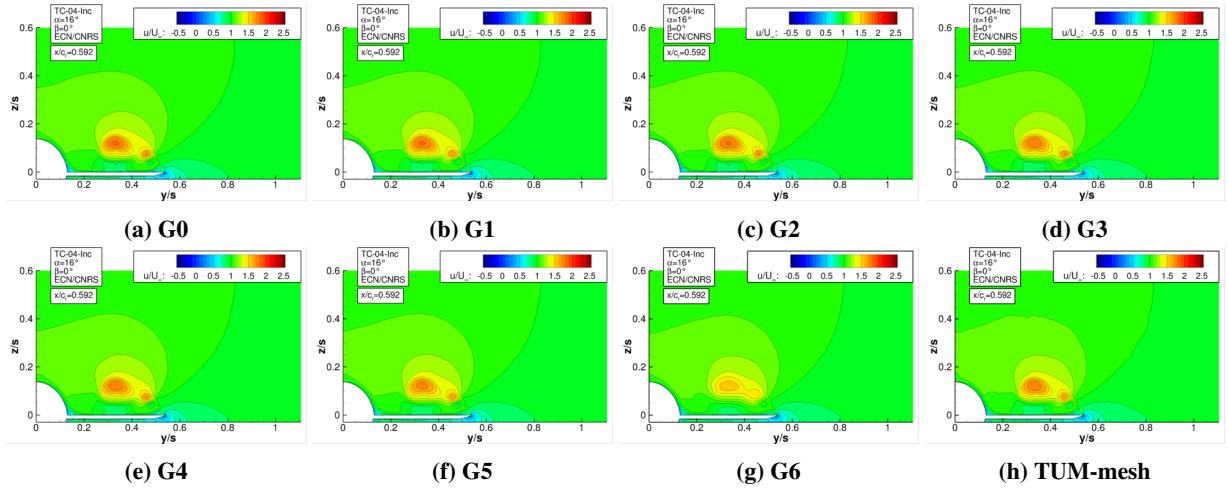

(a) G0 (b) G1 (c) G2 (d) G3

(e) G4 (f) G5 (g) G6 (h) TUM-mesh

Fig. 17 Dimensionless axial velocity at $x/c_r = 0.592$ vs the size of mesh for the NA1_W2 geometry for $\alpha = 16°$ and $\beta = 0°$; $Re = 3.0 \cdot 10^{-6}$ and $Ma = 0.15$.

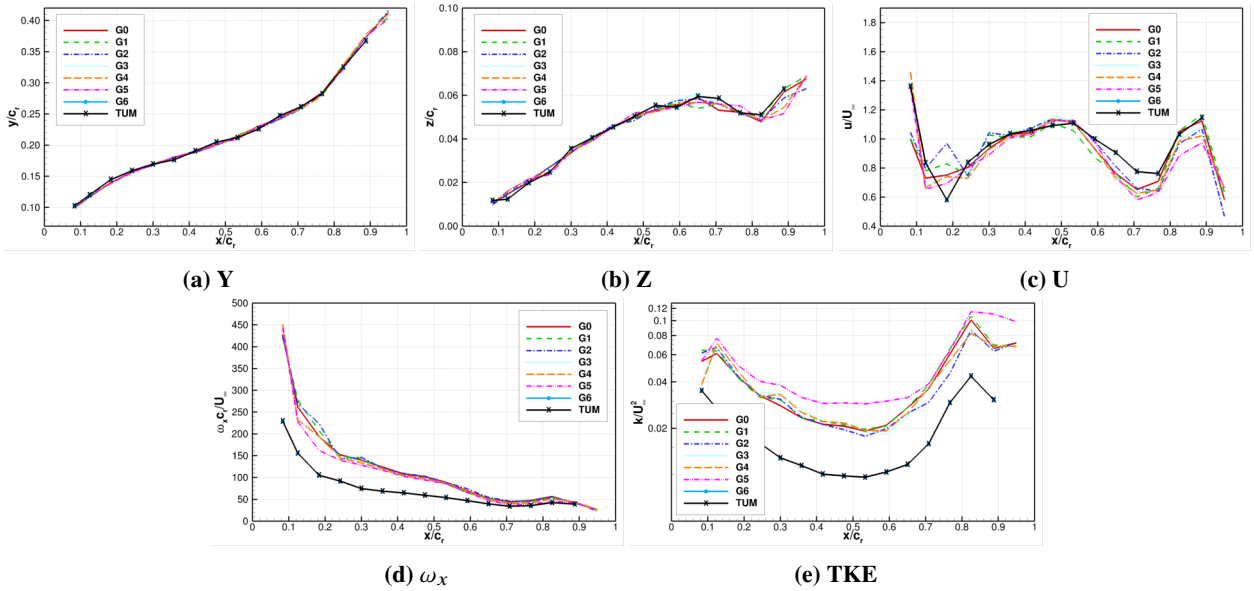

(a) Y (b) Z (c) U

(d) ω_x (e) TKE

Fig. 18 NA1_W1 - Grid sensitivity and Vortex Core Analysis for $\alpha = 16°$ and $\beta = 0°$; $Re = 3.0 \cdot 10^{-6}$ and $Ma = 0.15$.

rolling moment is not caused by grid sensitivity or modeling error. Regarding the DDES simulations, shown in the third and fourth lines, the combination of the DDES SST with the TUM grid provides the best agreement in the longitudinal characteristics and the lateral characteristics, excluding the rolling moment coefficient. In the DDES SA setup used by TUM, the lift and drag coefficients are predicted lower compared to the experimental data and the other simulation results. For the side force, pitching moment and yawing moment coefficient, the results are in a similar range as the simulations created with ISIS-CFD.

Table 4 shows data of the force and moment predictions obtained on these different grids for the NA1_W2 configuration. As for NA1_W1, the first two lines of this second table illustrate the non-negligible influence of the local grid density on the forces and moments. The results obtained with the k-ω SST closure on the flow-adapted grid (named "Hexpress+AGR") are closer to the experimental data, particularly, for the lift and drag coefficients. The k-ω SST with the Hexpress+AGR grid indicates the best agreement with the experimental data for most coefficients, even comparing it to the DDES SST and the DDES SA. The comparison between the k-ω SST and the DDES SST on the TUM grid shows

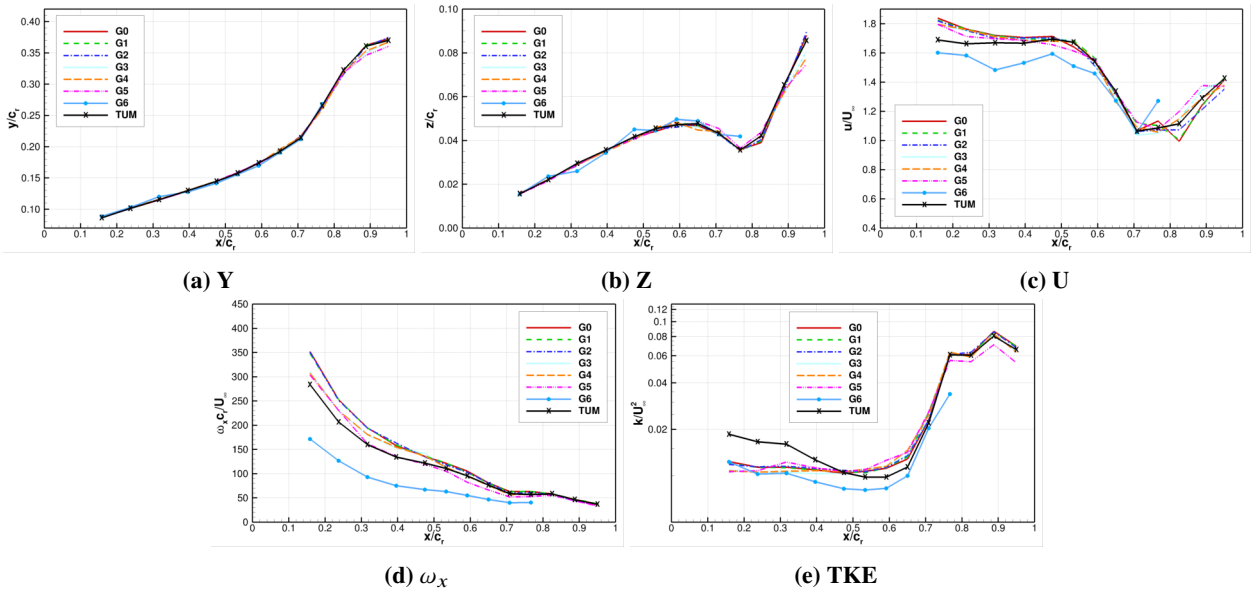

(a) Y **(b) Z** **(c) U**

(d) ω_x **(e) TKE**

Fig. 19 NA1_W2 - Grid sensitivity and Vortex Core Analysis for $\alpha = 16°$ and $\beta = 0°$; $Re = 3.0 \cdot 10^{-6}$ and $Ma = 0.15$.

Table 3 NA1_W1 - Forces and moments at $\alpha = 24°$ and $\beta = 5°$.

Model	Grid	C_D	C_S	C_L	C_{mx}	C_{my}	C_{mz}
Experiments		0.5724	0.0347	1.26231	-0.0024	0.1096	-0.0151
ISIS-CFD k-ω SST	Hexpress+AGR	0.5791	0.0426	1.2844	-0.0177	0.1011	-0.0120
ISIS-CFD k-ω SST	TUM	0.5219	0.0408	1.1554	0.0187	0.0896	-0.0186
ISIS-CFD DDES SST	Hexpress+AGR	0.5860	0.0389	1.3026	-0.0263	0.1100	-0.0110
ISIS-CFD DDES SST	TUM	0.5699	0.0385	1.2720	-0.0161	0.1075	-0.0127
TAU-CFD DDES SA	TUM	0.5483	0.0394	1.2252	-0.0103	0.1139	-0.0117

a significantly improved agreement of the DDES to experimental data. The solver and setup error is comparable due to the DDES SA and the DDES SST results on the TUM grid. The DDES SA is under-predicting and the DDES SST is over-predicting the lift and drag coefficients. The DDES SA exhibits a low agreement for the coefficients of side force, rolling and yawing moment for the NA1_W2 configuration.

Surface pressure distribution and skin friction lines. The surface pressure distributions provide a first assessment of the vortex behavior, interaction and breakdown and represent the connection between aerodynamic stability parameters and flow field patterns. Therefore, such data allow an inference of the origin of specific stability behaviors. Fig. 20 shows the surface pressure distribution and skin-friction lines obtained on the aforementioned combination of turbulence closures and grids for the NA1_W1 configuration. The influence of the grid density on the surface pressure distribution is obvious if one compares the two computations performed by the French authors on the two different grids with k-ω SST. The differences between the results of the hybrid RANS/LES model on the two grids are significantly alleviated. It is reassuring to notice that the computation performed with TAU on the TUM grid are similar to those made with ISIS-CFD on the same grid. Although the background RANS model is different (k-ω SST for ISIS-CFD and Spalart-Allmaras for TUM), the surface pressure field does not seem to be much affected by that at this level of detail. The most obvious differences are the vortex breakdown in the k-ω SST - TUM grid combination, see Fig. 20b at the windward wing. The surface pressures on the windward main wing are higher compared to the other setups, indicating a significantly more upstream vortex breakdown. This is the reason for the wrong prediction of the rolling moment in Table 3. Additionally, the streamlines in all DDES simulations indicate reversed flow close to the leeward trailing edge caused by a flow

Table 4 NA1_W2 - Forces and moments at $\alpha = 24°$ and $\beta = 5°$.

Model	Grid	C_D	C_S	C_L	C_{mx}	C_{my}	C_{mz}
Experiments		0.5657	0.0327	1.2403	0.0259	-0.0323	-0.0239
ISIS-CFD k-ω SST	Hexpress+AGR	0.5658	0.0368	1.2444	-0.0217	-0.0314	-0.0172
ISIS-CFD k-ω SST	TUM	0.5225	0.0391	1.1370	0.0065	-0.0209	-0.0220
ISIS-CFD DDES SST	TUM	0.5761	0.0394	1.2746	0.0134	-0.0435	-0.0164
TAU-CFD DDES SA	TUM	0.5543	0.0341	1.2137	0.0033	-0.0368	0.00120

separation.
Fig. 21 shows the same data for the NA1_W2 configuration and illustrates results obtained on the same grids and turbulence models already discussed for the NA1_W1 wing. The results show a similar flow behavior at the windward wing. The vortex breakdown is observable due to pressure increase in the rear wing region and at the main wing. This occurs significantly more upstream in Fig. 21b. Similar to the NA1_W1 configuration, the DDES simulations indicate reversed flow in the leeward rear wing area. Additionally, the high suction area in the DDES results indicates a more stable vortex system on the leeward side compared to the RANS results.

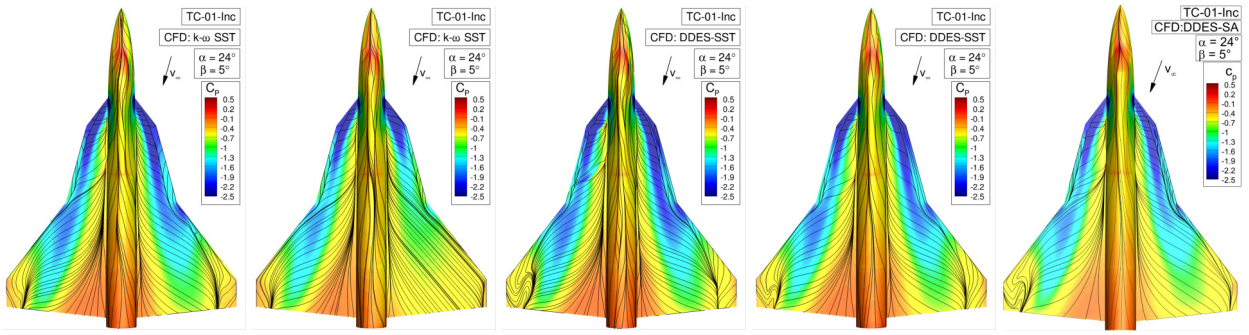

(a) ISIS-CFD k-ω SST Hexpress+AGR **(b) ISIS-CFD k-ω SST TUM-mesh** **(c) ISIS-CFD DDES Hexpress+AGR** **(d) ISIS-CFD DDES TUM-mesh** **(e) TAU DDES TUM-mesh**

Fig. 20 NA1_W1 - Surface pressure distribution C_p and skin friction lines at $\alpha = 24°$ and $\beta = 5°$; $Re = 3.0 \cdot 10^{-6}$ and $Ma = 0.15$.

For a more detailed comparison, the surface pressure distributions at different cross-sections are shown in Fig. 22. The first cross section at $x/c_r = 0.125$, see Fig. 22a features a different scale at the y-axis for an improved comparability. The distinct suction peaks of the IBV on each wing side are visible. The lower surface pressure at the windward side predicted by k-ω SST on the TUM mesh indicates an already burst vortex. Compared to the stable IBV in the k-ω SST - Hexpress+AGR, this behavior implies a high grid influence on the k-ω SST closure. This behavior occurs in all shown surface pressure cross sections. The low surface pressures on the windward side result in the high positive rolling moment, shown in Tab. 3. The DDES results are all exhibiting a similar suction peak, and are only varying in the development of the secondary vortex occurring close to the leading edge. Additionally, the IBV peak at the leeward side is slightly higher for DDES SA simulations. In the following sections, $0.475 < x/c_r < 0.823$, the suction peak reduces significantly for all numerical setups. The DDES SST and Hexpress+AGR combination features the highest negative surface pressure and the most pronounced secondary vortex peak. This can be attributed to the higher grid resolution compared to the TUM mesh and the improved prediction of the near-wall flow compared to RANS simulations.
The surface pressure distributions at four cross-sections for the NA1_W2 configuration are shown in Fig. 23. The different setups exhibit a similar behavior in the first slice, see Fig. 23a. Compared to the NA1_W1 configuration, the k-ω SST combined with the TUM mesh is more aligned with the other setups. The DDES SA and the DDES SST on the TUM mesh exhibit a similar behavior at the windward side, $y/s_{loc} > 0$, in all cross-sections. On the leeward side, the DDES SA features a continuously lower suction peak than the DDES SST. At $x/c_r = 0.592$, the suction peak in DDES SA is flattened due to the movement of a fuselage vortex below the wing vortex system. In the other setups, this flattened peak does not occur. This is because the trajectory of the fuselage vortex crosses the trajectory of the

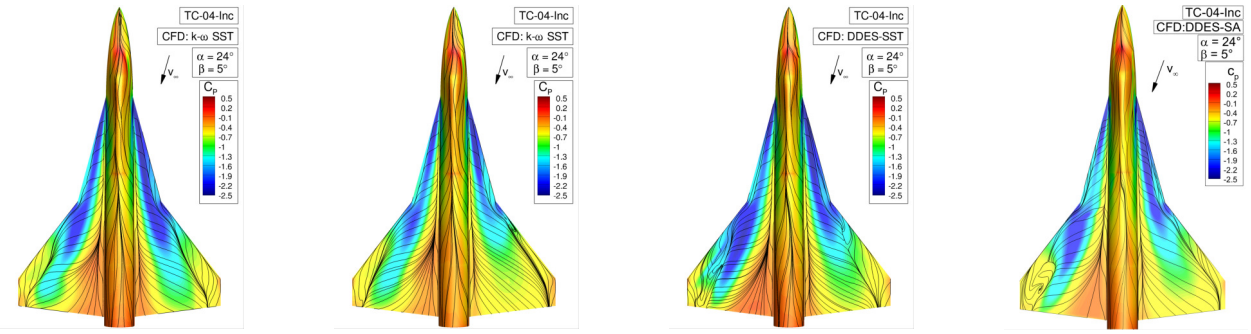

(a) ISIS-CFD k-ω SST Hexpress+AGR **(b) ISIS-CFD k-ω SST TUM-mesh** **(c) ISIS-CFD DDES TUM-mesh** **(d) TAU DDES TUM-mesh**

Fig. 21 NA1_W2 - Surface pressure distribution C_p and skin friction lines at $\alpha = 24°$ and $\beta = 5°$; $Re = 3.0 \cdot 10^{-6}$ and $Ma = 0.15$.

IBV more upstream. The differences between the k-ω SST on TUM and Hexpress grid show a high sensitivity to grid resolution, especially, on the windward side and in regions where the vortex system gets more unstable.
Fig. 22 (resp. Fig. 23) shows the surface pressure distribution at four cross-sections for the NA1_W1 (resp. NA1_W2) wing configuration. For both wing forms, the main alteration concerns the windward wing for which the k-ω SST cannot capture the local maximum observed on locally denser grids. The grid dependence is less marked on the leeward wing. Another unexpected observation is the grid sensitivity of the hybrid RANS/LES simulations. For both codes ISIS-CFD and TAU, the results seem to be less affected by the local grid density than to what is observed for the k-ω SST closure. However, on the windward wing, the highest surface pressure maximum is still reached on the flow-adapted grid.

Crosswise axial velocity distribution at $\mathbf{x/c_r = 0.592}$. Fig. 24 (resp. Fig. 25) depicts the dimensionless axial velocity distribution at $x/c_r = 0.592$ for the NA1_W1 (resp. NA1_W2) wing configuration. For NA1_W1, for the TUM grid, ISIS-CFD based on the k-ω SST closure predicts a very large wake-type IBV vortex and no MBV vortex on the windward wing at this cross-section. This complete vortex breakdown results in a high surface pressure, a positive rolling moment coefficient as well as an alleviated pitching moment coefficient. On the flow-adapted grid, the solution is totally different with a less pronounced wake-type IBV vortex and a well define jet-type MBV vortex. On the leeward side, the two solutions are very similar. The same trend, but less pronounced, can be observed when the DDES-SST hybrid RANS/LES is used: the wake-type IBV vortex is less diffused on the flow-adapted grid than on the TUM mesh. The TAU code and its DDES model employed on the TUM grid leads to a dimensionless axial velocity component roughly similar to what is provided by ISIS-CFD with its DDES closure and the same TUM grid. However, the windward IBV vortex appears less diffused and it has a larger wake-type vortex core than what is found by ISIS-CFD on the same grid with DDES-SST. These differences should be attributed to the different background RANS model used by the two teams. Anyway, none of the computations is able to capture the intense jet-like IBV leeward vortex revealed by the TUM experiments.
For NA1_W2, the simulation realized by ISIS-CFD on the TUM grid with k-ω SST has more diffused IBV vortices on both windward and leeward wings, underlining the same grid sensitivity. For instance, the windward MBV vortex is not visible on the TUM grid and the leeward wake-type core of the IBV vortex is surrounded by a zone with a more marked overshoot on the axial velocity component. This overshoot in axial as well as crossflow velocities and a high annular vorticity level surrounding the vortex core seem to be the reason for the higher surface pressure in the k-ω SST results. Moreover, the windward MBV vortex is clearly more visible on the flow-adapted grid. On the TUM grid, ISIS-CFD and TAU, using a hybrid RANS/LES model, predict a very similar velocity distribution, with more marked velocity overshoots for both vortices on the leeward side and for the MBV vortex on the windward side, for the TAU solution. This should be attributed to the differences on the RANS background closure. Both DDES models capture the flow characteristics similar to the PIV data.

Vortex core analysis. As discussed in subsubsection V.A.3 and emphasized in paragraph V.B.2, the vortex core flow characteristics are crucial for an accurate prediction of the flight stability characteristics. Therefore, a VCA is shown in Figs. 26 and 27. The location of the vortex core is obtained by the maximum axial vorticity for jet-type vortices and for

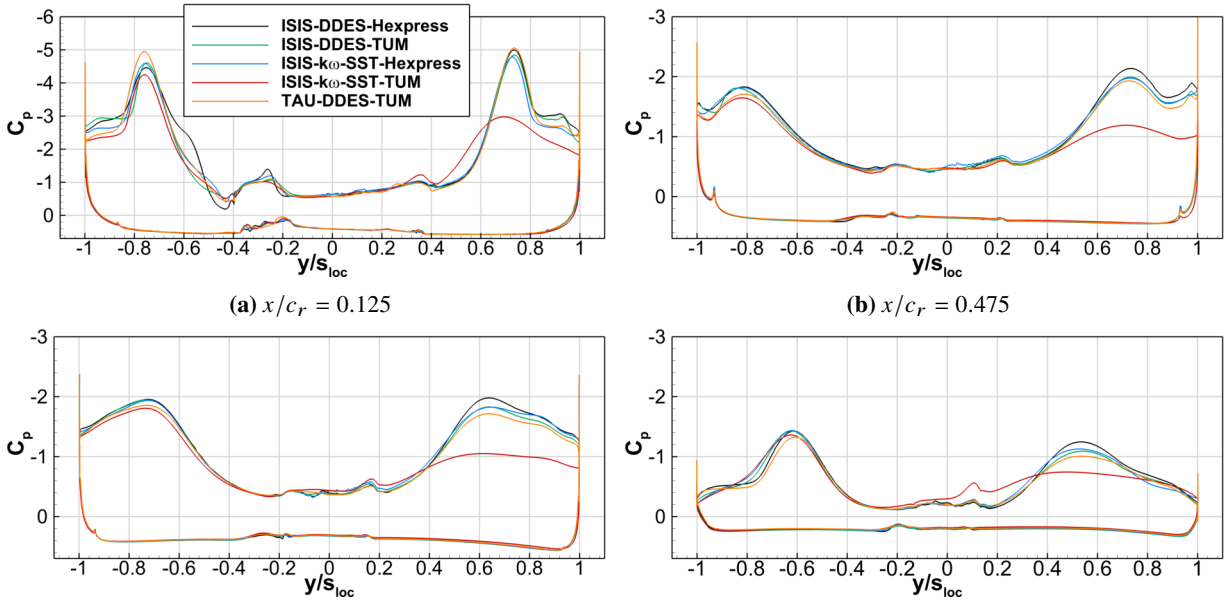

(a) $x/c_r = 0.125$ **(b)** $x/c_r = 0.475$

(c) $x/c_r = 0.592$ **(d)** $x/c_r = 0.825$

Fig. 22 NA1_W1 - Surface pressure distribution C_p at different cross-sections at $\alpha = 24°$ and $\beta = 5°$; $Re = 3.0 \cdot 10^{-6}$ and $Ma = 0.15$.

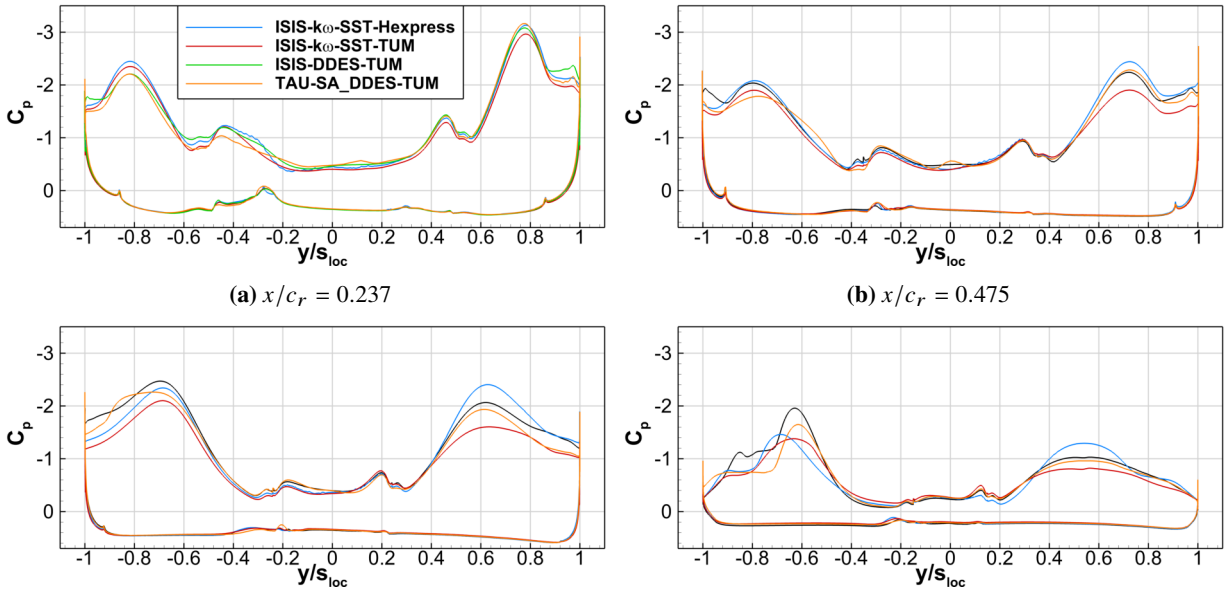

(a) $x/c_r = 0.237$ **(b)** $x/c_r = 0.475$

(c) $x/c_r = 0.592$ **(d)** $x/c_r = 0.825$

Fig. 23 NA1_W2 - Surface pressure distribution C_p at different cross sections at $\alpha = 24°$ and $\beta = 5°$; $Re = 3.0 \cdot 10^{-6}$ and $Ma = 0.15$.

wake-type vortices. The spanwise and vertical position as well as the non-dimensional axial velocity of the vortex core are presented in Fig. 24 for NA1_W1 configuration. The windward core characteristics are shown in Figs. 26a - 26c and the leeward side is presented in Figs. 26d - 26f. The y-position of the windward side is predicted well by the DDES simulations. The k-ω SST trajectories with both grids are more off from the experimental data due to the burst vortex and highly transient fluctuations in the vortex core. Therefore, the maximum vorticity is not necessarily located in the center of the circular area with higher vorticity. The vertical position of the IBV core predicted by the k-ω SST closure is located closer to the wing surface compared to experimental and DDES data. Particularly, the DDES SST with the flow-adapted grid and the DDES SA with the TUM mesh exhibit a similar trajectory. The velocities on the windward side indicate a vortex breakdown in the front wing area. All simulations exhibit reversed flow over the whole root chord, except the k-ω SST with the flow-adapted mesh. The MBV exhibits a steady decrease in axial core velocity. This is captured by all setups reasonably well. The leeward side features a stable vortex system in the front region and an experimentally determined breakdown position at $x/c_r \approx 0.62$. The simulations predict the trajectory in spanwise and vertical direction quite well including the vortex interaction and the MBVs inboard as well as downward movement. However, the DDES SST with the flow-adapted grid is the only setup predicting the vortex position in the rear wing correctly. The other setups predict a downward movement of the IBV. In the front wing, the axial core velocity is well predicted by DDES SA until the vortex breakdown at $x/c_r \approx 0.4$ indicating a more upstream breakdown compared to the experimental data. The ISIS-CFD solutions show a rather wake-type core flow along the whole root chord. The MBV core velocity is underestimated by all setups, but by the k-ω SST closures the most.

The NA1_W2 core flow exhibits a totally different behavior, see Fig. 27. As for the NA1_W1 configuration the windward core characteristics are presented in Figs 27a - 27c and the leeward characteristics in Figs 27d - 27f. On the windward side the IBV breaks down at $x/c_r \approx 0.5$ and the MBV at $x/c_r \approx 0.65$. The windward trajectory in spanwise as well as vertical direction is mostly predicted well. The k-ω SST closures show deficiencies regarding the trajectory after vortex breakdown. The axial core velocity is exceptionally well predicted by the DDES closures, especially the vortex breakdown is in very good agreement with the experimental data. The vortices on the leeward side interact strongly and the experimental data indicate a vortex merging at $x/c_r \approx 0.9$. The leeward side trajectory is again predicted in good agreement with the experimental results, especially the DDES SST with the TUM mesh is in very good agreement. The DDES SA trajectory diverges on the rear wing and the k-ω SST closures predict a downward movement of the IBV in the rear wing region. The axial core velocity, see Fig. 27f, is significantly underestimated by the k-ω SST closures. The hybrid RANS/LES models exhibit a better agreement with the experimental data. The DDES SA exhibits velocities close to the experimental results above the strake but a steep decrease above the main wing indicating vortex breakdown. This is also shown by the k-ω SST models. The DDES SST exhibits a stable vortex system and the best agreement with the experimental data.

The VCA shown in Fig. 26 (resp. Fig. 27) for the NA1_W1 configuration (resp. NA1_W2) exhibit a significant dependency to the turbulence closures and a higher grid sensitivity for the k-ω SST closures. The DDES setups show differences at the leeward side for the NA1_W1 configuration with a more stable IBV in the DDES SA setup. For the NA1_W2 configuration, the velocities in the jet-type IBV are predicted higher by DDES SA compared to DDES SST which can be attributed to the influence of the background RANS closure. The SA with rotation correction leads to a less diffused vortex core and therefore, in most cases to a more stable vortex and higher core velocities.

VI. Conclusion

In computational fluid dynamics (CFD), grid sensitivity and the impact of turbulence models are significant for the accuracy of numerical simulations. In this study, an extensive grid sensitivity analysis is conducted and the influence of modelling error regarding global and local flow characteristics is investigated. The considered configurations are a generic triple-delta-wing and a double-delta-wing configuration.

In a collaboration between Technical University of Munich (TUM), French National Centre for Scientific Research (CNRS) and the Centrale Nantes Engineering School (ECN), different grid types, turbulence models and solvers are compared. CNRS and ECN conducted simulations with the ISIS-CFD solver and performed grid adaptation which is based on the so-called flux-component Hessian criterion computed from Hessians of the pressure and velocity components. The grid sensitivity study is conducted on eight grids — seven grids with different resolutions generated by the French authors with an automatic grid refinement (AGR), and a hybrid grid introduced by the German authors. The TUM grid can be ranked between the second and fourth finest CNRS mesh depending on the scale used. The aerodynamic longitudinal stability characteristics resulting from simulations on different grids indicate well converged grids even for the coarser versions. However, the local vortex core flow characteristics exhibit major differences between

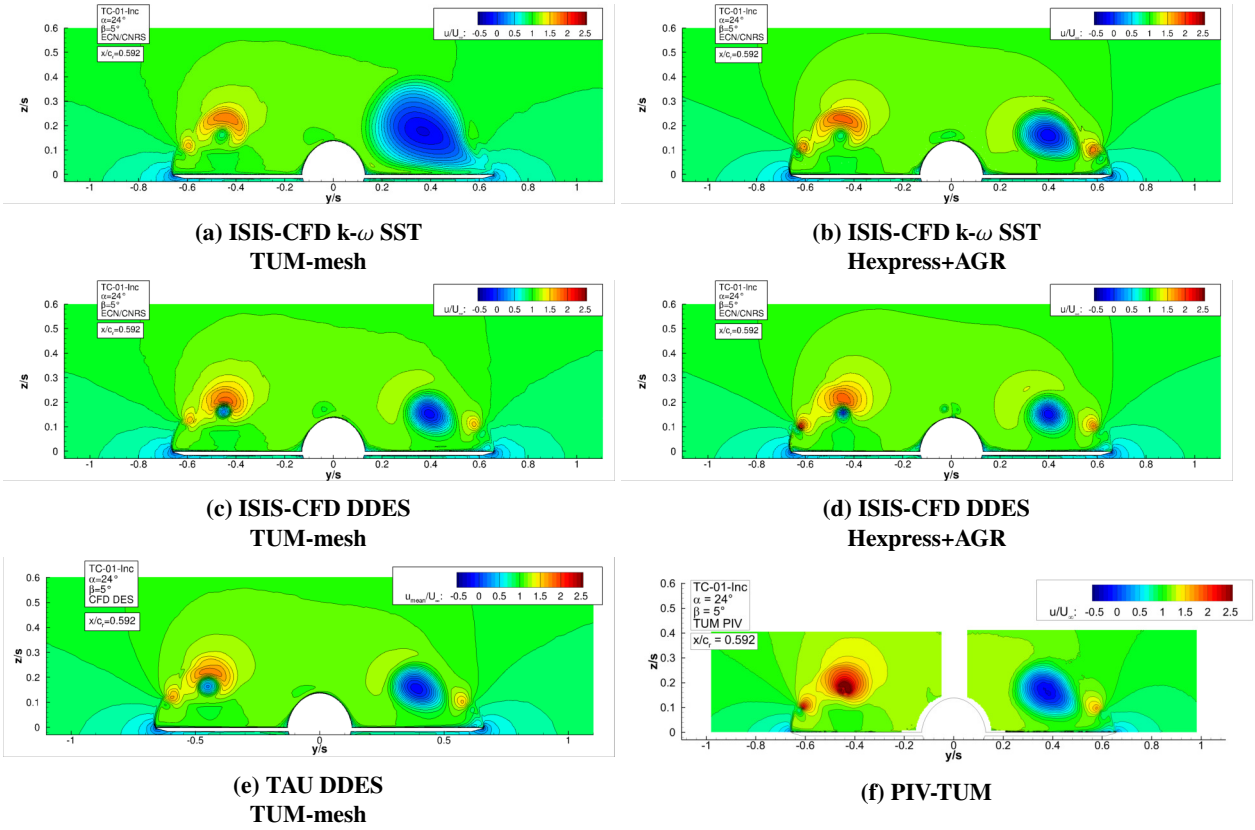

(a) ISIS-CFD k-ω SST TUM-mesh

(b) ISIS-CFD k-ω SST Hexpress+AGR

(c) ISIS-CFD DDES TUM-mesh

(d) ISIS-CFD DDES Hexpress+AGR

(e) TAU DDES TUM-mesh

(f) PIV-TUM

Fig. 24 NA1_W1 - Dimensionless axial velocity distribution at $x/c_r = 0.592$ for $\alpha = 24°$ and $\beta = 5°$; $Re = 3.0 \cdot 10^{-6}$ and $Ma = 0.15$.

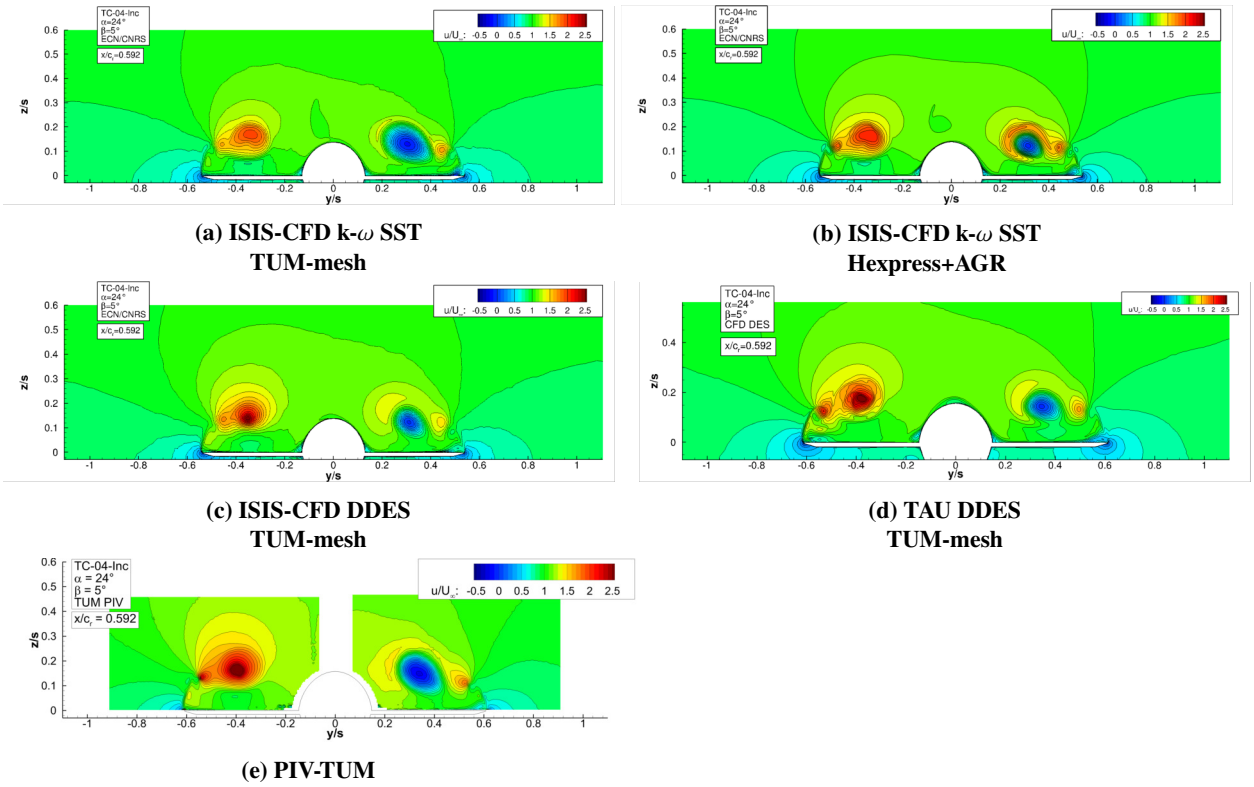

(a) ISIS-CFD k-ω SST TUM-mesh

(b) ISIS-CFD k-ω SST Hexpress+AGR

(c) ISIS-CFD DDES TUM-mesh

(d) TAU DDES TUM-mesh

(e) PIV-TUM

Fig. 25 NA1_W2 - Dimensionless axial velocity distribution at $x/c_r = 0.592$ for $\alpha = 24°$ and $\beta = 5°$; $Re = 3.0 \cdot 10^{-6}$ and $Ma = 0.15$.

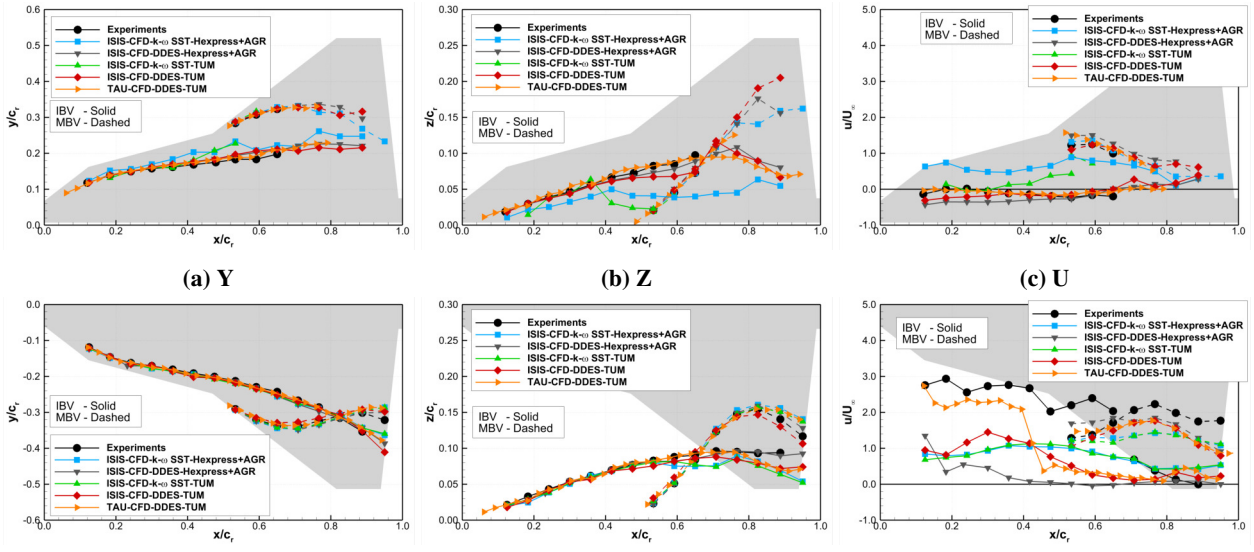

(a) Y

(b) Z

(c) U

(d) Y

(e) Z

(f) U

Fig. 26 NA1_W1 - Vortex core analysis by means of spanwise, y/c_r, and vertical z/c_r core position as well as nondimensional core-flow velocity u/v_∞ for $\alpha = 24°$ and $\beta = 5°$; $Re = 3.0 \cdot 10^{-6}$ and $Ma = 0.15$.

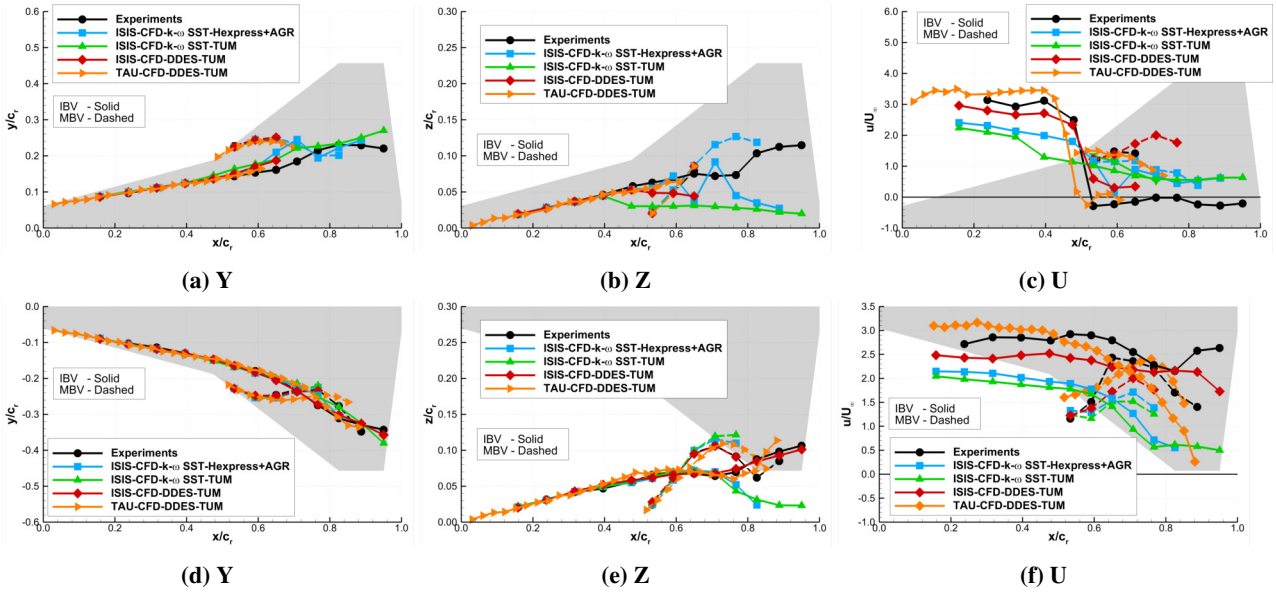

(a) Y **(b) Z** **(c) U**

(d) Y **(e) Z** **(f) U**

Fig. 27 NA1_W1 - Vortex core analysis by means of spanwise, y/c_r, and vertical z/c_r core position as well as nondimensional core-flow velocity u/U_∞ for $\alpha = 24°$ and $\beta = 5°$; $Re = 3.0 \cdot 10^{-6}$ and $Ma = 0.15$.

the grids. Especially, the results for the TUM mesh differs from the results on the AGR grids.
Therefore, a thorough and extensive study on grid sensitivity has to include a vortex core flow analysis (VCA) because the behavior in the vortex core strongly determines the accuracy of the moment prediction especially for lateral stability characteristics. This is also shown in the comparison of simulations to identify grid sensitivity and modelling errors. Here, simulations are performed for both configurations at an angle of attack of $\alpha = 24°$ and $\beta = 5°$. The simulations are performed with the two equation model k-ω SST, and a hybrid RANS/LES method used with SST by the French authors and SA by the German authors as background RANS closure. The French authors perform the simulations on a flow-adapted grid as well as on a hybrid TUM mesh. Comparing the results on both grids, the k-ω SST model shows a higher grid sensitivity than the DDES SST. The DDES results exhibit a better agreement to the experimental data and less differences between the meshes. However, the flow-adapted grid shows the highest resolution in the near-wall flow and the best agreement with the experimental data. For the triple-delta-wing configuration, the leeward inboard vortex (IBV) behavior is not captured by the simulations. On the one hand, experiments indicate a stable vortex system with a jet-type core. On the other hand, all simulations show a wake-type vortex core indicating a more upstream vortex breakdown onset. This leads to the previously discussed influence of the vortex core flow characteristics on the moment prediction. Due to the wake-type vortex core on the leeward side, the rolling moment exhibits a right wing up behavior. In the experimental data, the leeward IBV exhibits a jet-type core and therefore, induces a left wing up component to the rolling moment coefficient which is close to zero. The DDES simulations predict a similar flow field with differences regarding the level of diffusion in the vortex core caused by the background RANS closure.
For the doube-delta-wing configuration, flow field characteristics of the DDES are again in better agreement with the experimental data than the RANS model. But the k-ω SST simulation with the flow-adapted grid provided the best agreement with the experimental force and moment coefficients except for the rolling moment. This results from the higher surface pressure coefficient on the windward wing compared to other simulation setups which induces a right wing up component to the rolling moment — C_{mx} is alleviated. The good agreement on the longitudinal force and moment coefficients may be associated with an inaccurate prediction of different flow field patterns. This strengthens the statement proposed before that the grid sensitivity study and the comparison of numerical simulation data on vortex dominated flow field with experimental data has to include a VCA along with surface pressure distributions. Consequently, a good agreement to experimental data in the flight mechanics stability characteristics cannot be considered as sufficient to conclude on a good agreement for the vortex core characteristics.
Further investigations are needed to identify the reason for the more diffused vortex cores in the numerical results. This vortex core flow behavior results in an inaccurate prediction of the longitudinal and lateral stability characteristics and therefore, is crucial to requirements on the accuracy of the state-of-the-art CFD.

VII. Acknowledgements

The work performed by the ECN/CNRS authors was granted access to the HPC resources made available by GENCI of IDRIS and CINES under allocations in recurrent annual projects no. 00129. The project performed by the TUM authors is funded by the Deutsche Forschungsgemeinschaft (DFG, German Research Foundation) – grant number BR1511/13-1. The fruitful cooperation with Airbus Defense and Space is gratefully acknowledged. Furthermore, the authors thank the German Aerospace Center (DLR) for providing the DLR TAU-Code used for the numerical investigations. Moreover, the authors gratefully acknowledge the Gauss Centre for Supercomputing e.V. (www.gauss-centre.eu) for funding this project by providing computing time on the GCS Supercomputer SuperMUC at Leibniz Supercomputing Centre (www.lrz.de). The authors also highly appreciate the previous wind tunnel tests by Stefan Pfnür.

References

[1] Luckring, J. M., Park, M. A., Hitzel, S. M., Jirásek, A., Lofthouse, A. J., Morton, S. A., McDaniel, D. R., Rizzi, A., and Tomac, M., "Synthesis of Hybrid Computational Fluid Dynamics Results for F-16XL Aircraft Aerodynamics," *Journal of Aircraft*, Vol. 54, No. 6, 2017, pp. 2100–2114. https://doi.org/https://doi.org/10.2514/1.C034053.

[2] Hitzel, S., "Sub- and Transonic Vortex Breakdown Flight Condition Simulations of the F-16XL Aircraft," *Journal of Aircraft*, Vol. 31, No. 4, 2016, pp. 868–878. https://doi.org/https://doi.org/10.2514/3.46573.

[3] Pfnür, S., and Breitsamter, C., "Leading-Edge Vortex Interactions at a Generic Multiple Swept-Wing Aircraft Configuration," *Journal of Aircraft*, Vol. 56, No. 6, 2019, pp. 2093–2107. https://doi.org/https://doi.org/10.2514/1.C035491.

[4] Breitsamter, C., "Unsteady flow phenomena associated with leading-edge vortices," *Progress in Aerospace Sciences*, Vol. 44, No. 1, 2008, pp. 48 – 65. https://doi.org/https://doi.org/10.1016/j.paerosci.2007.10.002.

[5] Gursul, I., "Review of Unsteady Vortex Flows over Slender Delta Wings," *Journal of Aircraft*, Vol. 42, No. 2, 2005, pp. 299–319. https://doi.org/https://doi.org/10.2514/1.5269.

[6] Lofthouse, A. J., and Cummings, R. M., "Numerical Simulations of the F-16XL at Flight-Test Conditions Using Delayed Detached-Eddy Simulation," *Journal of Aircraft*, Vol. 54, No. 6, 2017, pp. 2077–2099. https://doi.org/10.2514/1.C034045.

[7] Shur, M. L., Strelets, M. K., Travin, A. K., and Spalart, P. R., "Turbulence Modeling in Rotating and Curved Channels: Assessing the Spalart-Shur Correction," *AIAA Journal*, Vol. 38, No. 5, 2000, pp. 784–792. https://doi.org/https://doi.org/10.2514/2.1058.

[8] Spalart, P. R., Deck, S., Shur, M., Squires, K., Strelets, M., and Travin, A., "A New Version of Detached-eddy Simulation, Resistant to Ambiguous Grid Densities," *Theoretical and Computational Fluid Dynamics*, Vol. 20, 2006, pp. 181–195. https://doi.org/https://doi.org/10.1007.

[9] Spalart, P. R., "Detached-Eddy Simulation," *Annual Review of Fluid Mechanics*, Vol. 41, No. 1, 2009, pp. 181–202. https://doi.org/https://doi.org/10.1146/annurev.fluid.010908.165130.

[10] Allmaras, S., Johnson, F., and Spalart, P., "Modifications and Clarifications for the Implementation of the Spalart-Allmaras Turbulence Model," *Seventh International Conference on Computational Fluid Dynamics (ICCFD7)*, 2012.

[11] Spalart, P., and Allmaras, S., *A one-equation turbulence model for aerodynamic flows*, 1992. https://doi.org/10.2514/6.1992-439.

[12] Queutey, P., and Visonneau, M., "An interface capturing method for free-surface hydrodynamic flows," *Computers & Fluids*, Vol. 36, No. 9, 2007, pp. 1481–1510.

[13] Leroyer, A., and Visonneau, M., "Numerical methods for RANSE simulations of a self-propelled fish-like body," *Journal of Fluids and Structures*, Vol. 20, No. 7, 2005, pp. 975–991.

[14] Deng, G. B., and Visonneau, M., "Comparison of explicit algebraic stress models and second-order turbulence closures for steady flows around ships," *In 7th International Conference on Numerical Ship Hydrodynamics*, 1999.

[15] Duvigneau, R., and Visonneau, M., "On the Role Played by Turbulence Closures in Hull Shape Optimization at Model and Full Scale," *J. Mar. Sci. Technol.*, Vol. 8, 2003, pp. 11–25.

[16] Cécora, R.-D., Radespiel, R., Eisfeld, B., and Probst, A., "Differential Reynolds-Stress Modeling for Aeronautics," *AIAA Journal*, Vol. 53, No. 3, 2015, pp. 1–17. Published online: 10 September 2014, March 2015.

[17] Guilmineau, E., Deng, B., G, Leroyer, A., Queutey, P., Visonneau, M., and Wackers, J., "Assessment of Hybrid RANS-LES Formulations for Flow Simulation around the Ahmed Body," *Computers & Fluids*, Vol. 176, 2015, pp. 302–319.

[18] Visonneau, M., Guilmineau, E., and Rubino, G., "Local Flow around a Surface Combatant at Various Static Drift Conditions: The Role Played by Turbulence Closures," *33rd Symposium on Naval Hydrodynamics*, Osaka, Japan, 2020.

[19] Wackers, J., Deng, G. B., Guilmineau, E., Leroyer, A., Queutey, P., and Visonneau, M., "Combined refinement criteria for anisotropic grid refinement in free-surface flow simulation," *Computers & Fluids*, Vol. 92, 2014, pp. 209–222.

[20] Mozaffari, S., Guilmineau, E., Visonneau, M., and Wackers, J., "Average-based mesh adaptation for hybrid RANS/LES simulation of complex flows," *Computers & Fluids*, Vol. 232, 2022, p. 105202.

[21] Menter, F. R., "Two-equation eddy viscosity turbulence models for engineering applications," *AIAA Journal*, Vol. 32, 1994, pp. 1299–1310.

[22] Gritskevich, M. S., Garbaruk, A. V., Schütze, J., and Menter, F. R., "Development of DDES and IDDES Formulations for the k-ω Shear Stress Transport Model," *Flow, Turbulence and Combustion*, Vol. 88, 2012, pp. 431–449.

[23] Pfnür, S., Hövelmann, A., Sedlacek, D., and Breitsamter, C., "Vortex Flow Interaction Phenomena on Multi Swept Delta Wings at Subsonic Speeds," *STO-MP-AVT-307, 20*, 2019.

[24] Raffel, M., Willert, C. E., Wereley, S. T., and Kompenhans, J., *Particle Image Velocimetry - A Practical Guide*, Springer Verlag, 2007.

[25] Sciacchitano, A., and Wieneke, B., "PIV Uncertainty Propagation," *Measurement Science and Technology*, Vol. Vol. 27, No. No. 8, 2016. https://doi.org/https://doi.org/10.1088/0957-0233/27/8/084006.

[26] Wackers, J., Deng, G. B., Guilmineau, E., Leroyer, A., Queutey, P., Visonneau, M., Palmieri, A., and Liverani, A., "Can adaptive grid refinement produce grid-independent solutions for incompressible flows?" *Journal of Computational Physics*, Vol. 344, 2017, pp. 364–380.